Journal of Visualisation manuscript No.
(will be inserted by the editor)

Effects of multiscale geometry on the large-scale coherent structures of an axisymmetric turbulent jet

Massimiliano Breda · **Oliver R. H. Buxton**

Received: date / Accepted: date

Abstract In this study the effect of multiscale geometry on the near-field structure of an axisymmetric turbulent jet is examined at a global Reynolds number of $Re_G = 10,000$. With the aid of tomographic particle image velocimetry (PIV), the suppression of the coherent structures due to this fractal geometry is analysed and the changes to the near-field vorticity are evaluated. This particular geometry leads to the break-up of the azimuthal vortex rings present for round jets and to the formation of radial and streamwise opposite-signed patches of vorticity. The latter are found to be responsible for the axis-switching of the jet, a phenomenon observed for some noncircular jets where the major axis shrinks and the minor one expands in the near field, effectively switching the two axes of the jet. This was the first time, to the knowledge of the authors, that axis-switching has been observed for a jet where the coherent structures have been suppressed. Following the significant differences found in the near field, the far field is examined. There, the integral lengthscale of the large scale eddies $\mathscr{L}_{ur}$ and the size of the jet evaluated in terms of the jet half-width $r_{1/2}$ are found to evolve in a similar fashion, whilst the ratio $\mathscr{L}_{ur}/r_{1/2}$ is found to be higher for the fractal jet than for the round jet, for which the near-field structures have not been suppressed.

Keywords Axisymmetric jet · Coherent Structures · Tomographic PIV · Multiscale geometry · Noncircular jet

1 Introduction

Previous studies have investigated the role of the coherent structures (the so called Kelvin-Helmholtz vortex rings) in an axisymmetric round jet. As shown by Yule (1978) and Dimo-

Mr M. Breda
Department of Aeronautics
Imperial College London
London (UK)
E-mail: mb2014@ic.ac.uk

Dr O. R. H. Buxton
Department of Aeronautics
Imperial College London
London (UK)
E-mail: o.buxton@imperial.ac.uk

takis et al (1983), vortex rings are emitted at the exit of a round jet and these large-scale structures are important for both entrainment and mixing. Since the 1980s, various authors have tried to modify the state of these coherent structures in order to obtain entrainment and mixing benefits. It was found that both large wetted perimeter (Shakouchi and Iriyama, 2014) and a combination of corners and flat sides (Gutmark et al, 1989) would allow the augmentation of both. Hence a repeating fractal pattern (fractal dimension $D_f = 1.5$ and 3 iterations) is proposed, which maximises the number of corners and wetted perimeter for a given open area. The same geometry has been studied for axisymmetric wake generators (Nedić et al, 2013), where a break-up of the coherent structures and a reduction of the shedding energy were observed. We therefore examine round and fractal orifices to investigate the effects on the near and far field due to the different embedded coherence with the aid of planar and tomographic particle image velocimetry (PIV). The repetitive fractal pattern is applied to a base square geometry, leading to a different aspect ratio $\mathcal{AR}$, defined as

$$\mathcal{AR} = \frac{\text{Major Axis}}{\text{Minor Axis}}. \tag{1}$$

2 Methodology

The experiments are conducted in a jet facility at Imperial College London. The air flow is conditioned with a honeycomb and two screens of decreasing mesh size before it enters a 5^{th} order polynomial contraction leading to a turbulence intensity of 0.5% at the centreline. Two orifices of identical open area (D_e^2), as shown in Figure 1, were attached to the jet exit. The flow was evaluated using a cylindrical coordinate system (x, r, θ), as shown in Figure 2a. Initially, a low resolution two-dimensional two-component (2D-2C) planar particle image

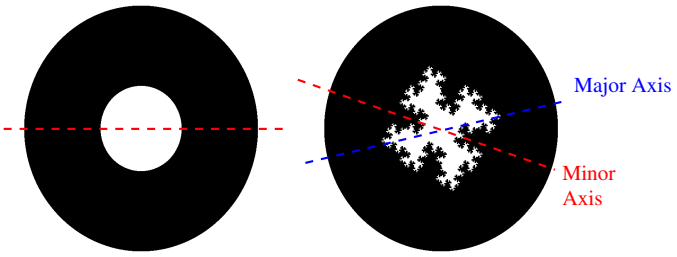

(a) Round ($\mathcal{AR}$= 1) (b) Fractal ($\mathcal{AR}$= 2.5)

Fig. 1: Exit geometries studied, major axis and minor axis are shown.

velocimetry (LRPIV) was conducted across the $x-r$ plane between 0 and 23 D_e, placing the laser sheet across the jet's centreline, where D_e is the equivalent diameter of the orifices and U_e the equivalent velocity

$$D_e = \sqrt{\text{Exit area}} = 15.8\,\text{mm} \qquad U_e = \frac{\text{Volumetric flow rate}}{\text{Exit area}} = 9.93\,\text{m/s}. \tag{2}$$

For the fractal jet, tests were conducted across both major and minor geometrical axes, as shown in Figure 1. Henceforth, "major" and "minor" axes will specifically refer to the planes aligned with their respective axes at the jet exit. An Imager SX 4M camera was used for the acquisition. In total, 1,500 images were acquired per jet configuration. Subsequently, a high resolution planar PIV (HRPIV) experiment was conducted between 23 and 26 x/D_e, to study the effect of the exit geometries on the turbulent lengthscales of the jet in the far field. This time, 4,500 images were acquired using the same camera. Following the findings from these two experiments, 3D-3C tomographic PIV (TPIV) (Elsinga and Scarano, 2006) was conducted in a slice of the jet of thickness 5 mm, perpendicular to the $r-\theta$ plane, with 1,500 images acquired (U_x is the out-of-plane component), imaging the flow in forward scatter using four cameras Imager SX 4M. All experiments were conducted at a global Reynolds number of $Re_G = 10,000$, where

$$Re_G = \frac{U_e D_e}{\nu}. \tag{3}$$

The laser sheet (or volume for the TPIV case) was produced in both experiments by a low speed double cavity Nd:YAG laser at 15 Hz, whilst the image processing was done in the commercial software DaVis 8.4. A summary of the processing steps of the experiments is detailed in Table 1. The TPIV images were processed using the MART algorithm (6

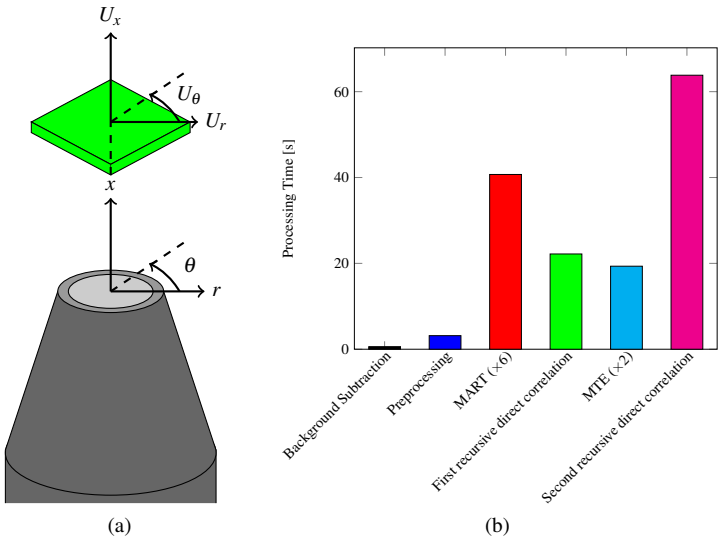

(a) (b)

Fig. 2: (a) Jet's schematics and position of TPIV volume. (b) Processing time of a single TPIV time step in DaVis. The computer has two processors Intel(R) Xeon(R) CPU ES-2690 v2 at 3 GHz and 128 GB of RAM.

iterations), a multiplicative algebraic reconstruction (Herman and Lent, 1976). In order to improve the quality of the reconstruction, the dark background previously acquired was subtracted. Sliding minimum subtraction, Gaussian smoothing using a 3×3 pixels kernel (to reduce the background noise) and sharpening (to reduce the number of ghost particles) were also performed on the raw images, allowing the particle diameter to be of the order of 2

pixels and the ppp to be within 0.04 and 0.05. Volume self-calibration (Wieneke, 2008) was then applied to the reconstructed particle-image volumes to improve the data accuracy. In order to reduce the postprocessing time sparse cross-correlation (Discetti and Astarita, 2012) was implemented. The vectors were reconstructed in three steps: an initial recursive direct correlation[A], followed by two iterations of motion tracking enhancement (MTE) (Novara et al, 2010) to reduce the number of ghost particles and a final recursive direct correlation[B]. A summary of the processing steps together with the computational time is provided in Figure 2b. Finally, in order to correct the non-zero divergence, the data were corrected using the divergence correction scheme (DCS) as in De Silva et al (2013). This scheme is based on a non-linear optimisation based constraint which minimally alters the acquired velocity field, whilst restricting the magnitude of the divergence to a maximum tolerance. The objective function to be minimised is the ensemble average of the "turbulent kinetic energy" added to the measured velocity field, i.e. $\tilde{k} = \sum_{i=1}^{3} \langle (U_i - \overline{U}_i) \rangle$, where the velocity is split following the Reynolds decomposition as:

$$U_i = \overline{U}_i + u_i. \tag{4}$$

The divergence error was set to be $|\partial \tilde{u}_i / \partial x_i \leq 10 s^{-1}|$ [C] after a convergence study, which led to an average $\tilde{k}/\overline{U}_{cl} < 5\%$ (compensated by the jet streamwise centreline velocity).

Finally, the experiments' spatial resolution was evaluated by estimating the dissipation rate ε using all nine velocity gradients (George and Hussein, 1991) from the TPIV data and deriving the Kolmogorov lengthscale $\eta = (\nu^3/\varepsilon)^{1/4}$. Additionally, a HRPIV test was conducted in the near field, $2 \leq x/D_e \leq 6$, in order to estimate the dissipation rate since a spatial resolution, in terms of cross-correlation window, that is twice as fine as that of the TPIV could be achieved. The resolution of this HRPIV data was estimated to be between $6-9\eta$ (worst case). The dissipation rate estimated from the TPIV data set and the HRPIV data set, using the assumption of local axisymmetry (George and Hussein, 1991), were found to differ by up to 50% due to the coarse spatial resolution of the TPIV. In fact both estimates of dissipation are likely to be underestimates since a resolution of $\sim 3\eta$ is considered necessary to resolve the dissipative scales of a turbulent flow (Worth et al, 2010; Buxton et al, 2011). Nevertheless, in terms of the longitudinal Taylor lengthscale λ_f, the spatial resolution of the TPIV was always less than $0.6\lambda_f$, which is deemed more than sufficient to resolve the large-scale vortical structures, which are the focus of this study.

Table 1: Processing details for Planar and Tomographic PIV

	LRPIV	HRPIV	TPIV
Initial interrogation window	64×64 pixels	64×64 pixels	$160 \times 160 \times 160$ voxels
Final interrogation window	16×16 pixels	12×12 pixels	$48 \times 48 \times 48$ voxels
Overlap	50%	50%	75%
Spatial resolution (worst case)	22η	5.5η (far field)	11η
Digital Resolution (px/mm)	16.7	28.0	45.7

[A] The first recursive direct correlation was done in steps of specific correlation volume voxel size (passes): $160 \times 160 \times 160(10) \rightarrow 96 \times 96 \times 96(2) \rightarrow 64 \times 64 \times 64(2)$. The volume overlap was 75%.

[B] The second recursive direct correlation was: $160 \times 160 \times 160(10) \rightarrow 96 \times 96 \times 96(2) \rightarrow 64 \times 64 \times 64(2) \rightarrow 48 \times 48 \times 48(2)$. The volume overlap was 75%.

[C] The notation $\tilde{\cdot}$ is used to denote the corrected velocity field for tomographic PIV after the DCS is applied. Later it is dropped since the analysis on the 3D-3C data is based solely on the corrected fields.

3 Results

Since the work of Brown and Roshko (1974), coherent structures have attracted numerous studies, however the terminology "coherent structures" itself did not receive a formal definition until the work of Hussain (1986): *a connected turbulent fluid mass with instantaneously phase-correlated vorticity over its spatial extent*. This motivated the acquisition of the full three-dimensional vorticity vector to study and evaluate the state of such structures. Despite the sole availability of 2D PIV data, Breda and Buxton (2017) suggested that the fractal geometry would lead to a break-up of the coherent structures for an axisymmetric jet, evidenced by the suppression of the negative anti-correlation in the two-point correlation between the radial velocity component v in the streamwise direction x, usually associated with the Kelvin-Helmholtz (K-H) vortex rings. In this study, we further investigate the state of the coherent structures by analysing the vorticity, calculated from the tomographic PIV data, in polar coordinates $\omega = [\omega_r, \omega_\theta, \omega_x]$. An initial evaluation can be done by looking at the time averaged mean vorticity in the near field across all time steps acquired

$$|\overline{\omega}| = \overline{\sqrt{\omega_r^2 + \omega_\theta^2 + \omega_x^2}} \tag{5}$$

compensated by the jet streamwise centreline velocity $\overline{U}_{cl}$ and jet half-width $r_{1/2}$ defined as,

$$\overline{U}_x(x, r_{1/2}) = 0.5\overline{U}_{cl}(x). \tag{6}$$

For an axisymmetric round jet, it is expected that the coherent structures will appear as a coherent region of vorticity surrounding the jet core, due to the development of the K-H vortex rings. This is presented in Figure 3. For the fractal jet, the multiscale geometry generates isolated areas of high absolute vorticity, even though it appears there is still a largely coherent ring of vorticity around its core, as shown in Figure 3b. However, in order to complete the analysis on the state of the coherent structures, the single components of vorticity need to be analysed. In fact, as discussed by Violato and Scarano (2011), modifying the state of coherence using a chevron nozzle led to a reduction of the azimuthal vorticity ω_θ and to an increase of the importance of the radial ω_r and streamwise ω_x components. Hence, the orientation of the vorticity vector is now evaluated to verify that the large scale vorticity remains coherent across at least one component.

The first component to be investigated is ω_θ, which is the dominant one of the K-H vortex rings for a round jet. As shown by the contour of mean ω_θ in Figure 4a, the coherence of the round jet is shown by a well-defined ring of vorticity. Further, it is confirmed that most of the contribution to the overall mean vorticity is due to the azimuthal vorticity, since the radial and streamwise components are negligible in comparison, as shown in Figure 5a and Figure 6a

$$|\omega_\theta| \gg |\omega_r| \approx |\omega_x| \approx 0. \tag{7}$$

Having shown a clear example of coherent vorticity, the fractal jet is now evaluated. Differently from the round jet, this time the azimuthal vorticity is found to be split into patches of strong vorticity as shown in Figure 4b, which are divided by the fractal geometry. The suppression of coherence leads to the formation of opposite-signed radial patches of vorticity as shown in Figure 5b, with magnitude significantly higher compared to the round jet. These patches are found to form uniformly around the core of the fractal jet. Patches of opposite-signed streamwise vorticity, of lower intensity compared to the radial component, are also observed in Figure 6b

$$|\omega_\theta| \simeq |\omega_r| \gtrsim |\omega_x|. \tag{8}$$

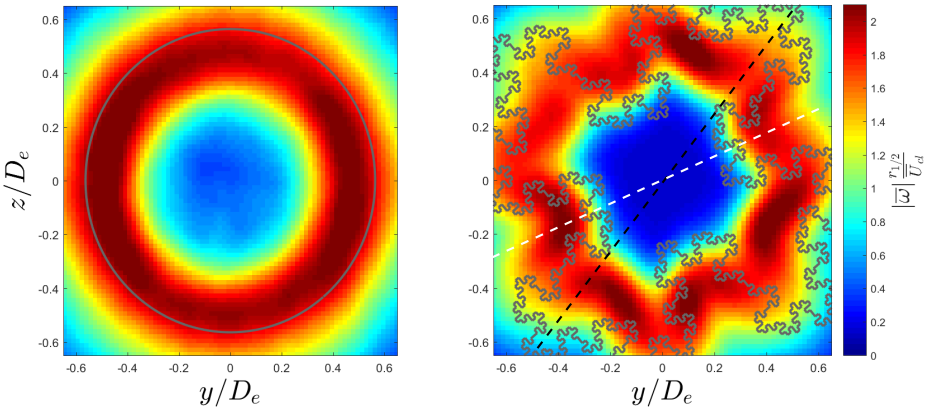

(a) Round (b) Fractal

Fig. 3: Mean vorticity $|\overline{\omega}|$ at $x/D_e = 2$, the exit geometry is shown in grey (TPIV data). The major axis (black dashed line) and the minor axis (white dashed line) are shown for the fractal jet.

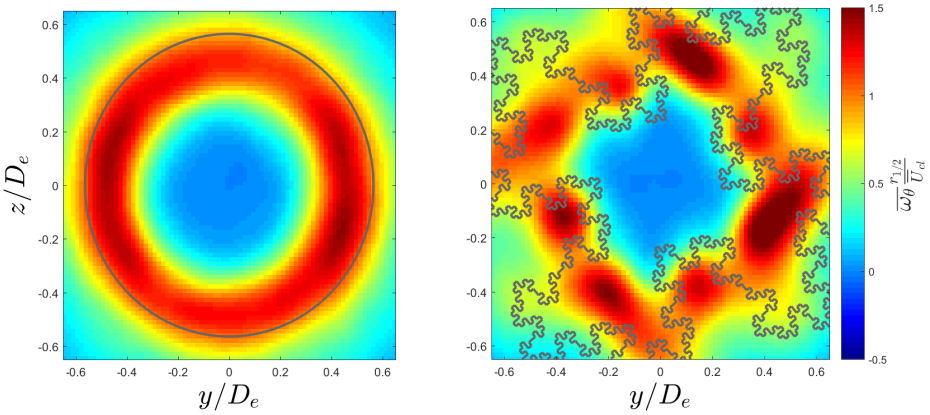

(a) Round (b) Fractal

Fig. 4: Mean azimuthal vorticity ω_θ at $x/D_e = 2$ (TPIV data)

As shown, none of the vorticity vector components show a coherent behaviour, since the azimuthal vorticity is split into patches, whilst the streamwise and radial ones are divided into areas of opposite sign. Hence, following the definition of Hussain (1986), no large-scale coherent structures can be found in the mean, suggesting the multiscale geometry is responsible for suppressing them. Of particular interest is the distribution of ω_x and ω_θ, which have been found before to promote "axis-switching". This phenomenon, where the major axis of the noncircular jet shrinks as the minor one expands, has been previously reported for square

jets (Quinn, 1992; Zaman, 1996), but it has not been observed for jets where the coherence was suppressed due to, for example, the fractal geometry. A first observation can be drawn from Figure 3b, where it is observed that the regions of high vorticity across the major axis are moving towards the jet centre compared to the exit geometry, while the ones across the minor axis are expanding away from the core. In Figure 8a, axis-switching is identified too at $x/D_e = 2.3$, at which the jet half-width imaged across the major axis for the fractal jet becomes smaller than the one at the minor axis. This phenomenon has been found for various

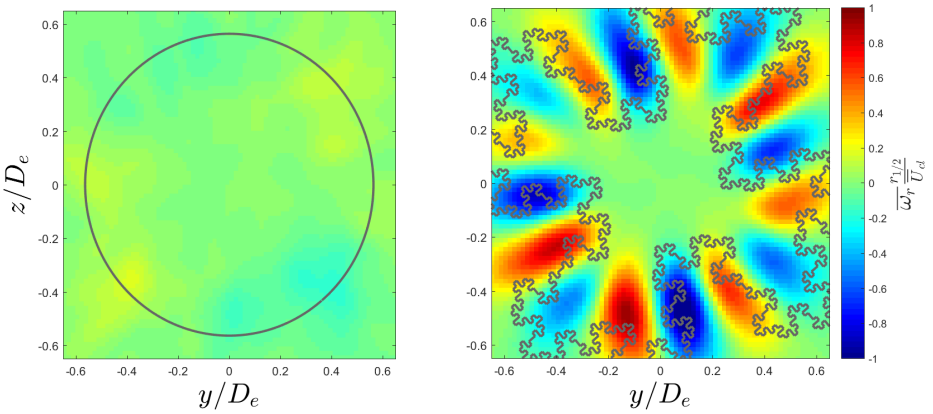

(a) Round (b) Fractal

Fig. 5: Mean radial vorticity ω_r at $x/D_e = 2$ (TPIV data).

noncircular jets and it was explained through the contribution of ω_θ (Hussain and Husain, 1989) and ω_x (Zaman, 1996). The former was mainly linked to the different induced velocity between the major and the minor axes across an elliptical vortex ring, leading to the faster segments curling up and protruding from the jet core. For the fractal jet at issue, however, this appears not to be the leading cause of axis-switching due to the break-up of the azimuthal vorticity. The study of Zaman (1996), who tested rectangular jets fitted with tabs alternatively on the major or on the minor axes, suggested that axis-switching would take place only if the non-circular geometry emitted regions of opposite-signed streamwise vorticity with the signs as in Figure 7b, where flow would be injected towards the jet centre, thereby shrinking the major axis. However, if the signs of the streamwise vorticity were as in Figure 7a, the flow would be ejected towards the ambient and therefore axis-switching would not occur. As shown in Figure 6b, the fractal geometry generates regions of opposite-signed streamwise vorticity, whose direction makes them inject fluid towards the jet centre, indicating that for this jet the ω_x dynamics is likely responsible for the axis-switching. ω_x does not exclude a relevant contribution of ω_θ too, since its asymmetrical distribution could also be responsible for this phenomenon. However, the streamwise vorticity certainly plays the key role of shrinking the major axis, allowing this phenomenon to take place.

Despite the significant differences in the near field, it remains to be clarified if the coherent structures have any residual effect in the far field, where the jet is fully developed. Since the work of Townsend (1976), it has been believed that flows would achieve self-

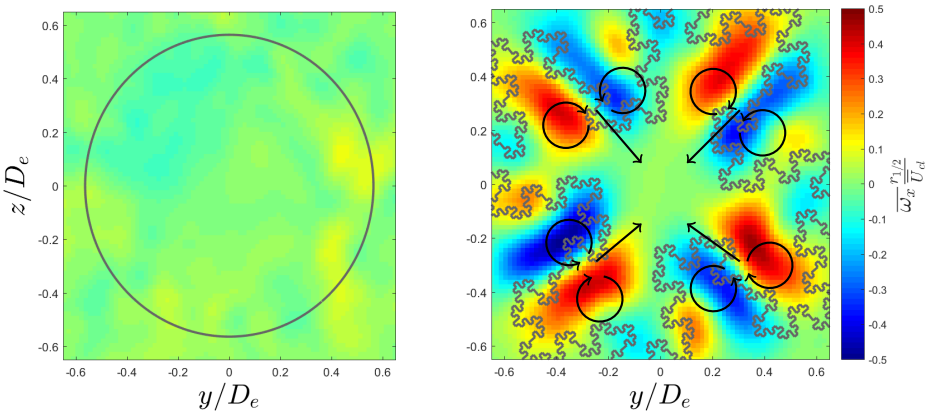

(a) Round (b) Fractal

Fig. 6: Mean streamwise vorticity $\omega_x$at $x/D_e = 2$. The opposite-signed vortex regions leading to the axis-switching are shown by the arrows (TPIV data).

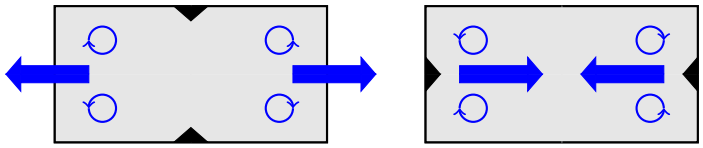

(a) No axis-switching (b) Axis-switching

Fig. 7: Schematics of the jets fitted with tabs from Zaman (1996).

similarity, becoming independent of the initial conditions (i.e. independent from the state of the near-field coherent structures), due to the entrainment of background fluid into the turbulent stream. George (1989) suggested even that the initial conditions could affect the spreading rate of the jet but not the self-similar profiles. In order to further investigate the influence of the coherent structures in the far field, the region between 23 and 26 x/D_e is examined, where the mean velocity and Reynolds stresses are found to be self-similar. We do so by evaluating the integral lengthscale $\mathscr{L}_{ur}$, calculated at the jet centreline from the jet two-point correlation R_{ur} of the streamwise velocity fluctuations u in the radial direction r. Due to the limited size of the field of view, the integration was performed between $r = 0$ and the first zero-crossing r', which has been confirmed to be sufficient for an integral scale evaluation by Nicolaides et al (2004).

$$R_{ur}(x,r,\psi) = \frac{\langle u(x,r)u(x,r+\psi)\rangle}{u'(x,r)u'(x,r+\psi)} \tag{9}$$

$$\mathscr{L}_{ur}(x) = \int_0^{r'} R_{ur}(x,\psi)\mathrm{d}\psi \tag{10}$$

The integral lengthscale $\mathscr{L}_{ur}$, which represents the size of the large scale turbulent eddies, is compensated by the jet half-width $r_{1/2}$, which can be interpreted as the macroscopic length-

scale of the jet as a whole. As shown in Figure 8b, the ratio $\mathscr{L}_{ur}/r_{1/2}$ is a constant for both

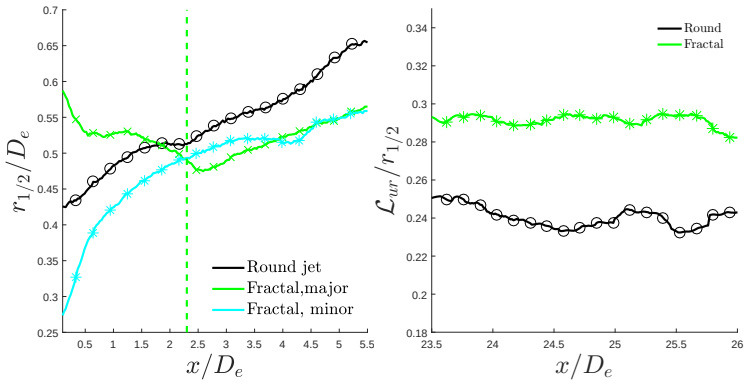

(a) (b)

Fig. 8: (a) Axis-switching in the near field (LRPIV data) and (b) $\mathscr{L}_{ur}/r_{1/2}$ in the far field (HRPIV data). The location of the axes-switch is shown by the green dashed line. A marker is plotted every 10 points to avoid clutter.

jets (verifying an assumption made in George (1989)), indicating that the large-scale eddies and the whole jet are evolving in a similar fashion to one another. However, this constant is larger for the fractal jet. This suggests that traces of the suppression of the coherent structures can be found in the far field, even though the jet is evolving independently of the initial conditions.

4 Conclusions

In this study, the effects of suppressing the coherent structures with the aid of multiscale-fractal geometry have been investigated. It is found that the fractal geometry breaks up the coherent vortex rings as shown by the azimuthal vorticity and by the mean vorticity, however it also re-orients the vorticity vector, increasing the magnitude of ω_r and ω_x. The latter is found to play a key role for the axis-switching of the fractal jet due to the opposite-signed patches of vorticity injecting fluid towards the jet centre. Despite the significant differences in the near field, it is observed that the eddies and the jet half-width evolve in a similar fashion in the far field. However, the suppression of coherence is still visible in the ratio between $\mathscr{L}_{ur}$ and $r_{1/2}$ in the far field, which is observed to be higher for the fractal jet.

Acknowledgements The authors gratefully acknowledge EPSRC for funding through EPSRC grant no. EP/L023520/1.

References

Breda M, Buxton ORH (2017) Near and far-field analysis of an axisymmetric fractal-forced turbulent jet. In: Örlü R, Talamelli A, Oberlack M, Peinke J (eds) Prog. Turbul. VII,

Springer International Publishing, pp 211–217
Brown GL, Roshko A (1974) On density effects and large structure in turbulent mixing layers. J Fluid Mech 64:775–816
Buxton ORH, Laizet S, Ganapathisubramani B (2011) The interaction between strain-rate and rotation in shear flow turbulence from inertial range to dissipative length scales. Phys Fluids 23(6):1–4
De Silva CM, Philip J, Marusic I (2013) Minimization of divergence error in volumetric velocity measurements and implications for turbulence statistics. Exp Fluids 54(7):1–17
Dimotakis PE, Miake-Lye RC, Papantoniou DA (1983) Structure and dynamics of round turbulent jets. Phys Fluids 26(11):3185–3192
Discetti S, Astarita T (2012) Fast 3D PIV with direct sparse cross-correlations. Exp Fluids 53:1437–1451
Elsinga GE, Scarano F (2006) Tomographic particle image velocimetry. Exp Fluids 41(6):933–947
George WK (1989) The Self-preservation of turbulent flows and its relation to initial conditions and coherent structures. Tech. rep., University at Buffalo, Buffalo, New York, USA
George WK, Hussein HJ (1991) Locally axisymmetric turbulence. J Fluid Mech 233:1–23
Gutmark E, Schadow KC, Parr T (1989) Noncircular jets in combustion systems. Exp Fluids 7:248–258
Herman GT, Lent A (1976) Iterative Reconstruction Algorithms. Comput Biol Medision 6:273–294
Hussain AKMF (1986) Coherent structures and turbulence. J Fluid Mech 173:303–356
Hussain F, Husain HS (1989) Elliptic jets. I - Characteristics of unexcited and excited jets. J Fluid Mech 208:257–320
Nedić J, Vassilicos JC, Ganapathisubramani B (2013) Axisymmetric turbulent wakes with new nonequilibrium similarity scalings. Phys Rev Lett 111(144503):1–5
Nicolaides D, Honnery DR, Soria J (2004) Autocorrelation Functions and the Determination of Integral Length with Reference to Experimental and Numerical Data. 15th Australas Fluid Mech Conf 1(December):1–4
Novara M, Batenburg KJ, Scarano F (2010) Motion tracking-enhanced MART for tomographic PIV. Meas Sci Technol 21(035401):1–18
Quinn WR (1992) Streamwise evolution of a square jet cross section. AIAA J 30(12):2852–2857
Shakouchi T, Iriyama S (2014) Flow characteristics of submerged free jet flow from petal-shaped nozzle. J Fluid Sci Technol 9(3):1–7
Townsend AA (1976) The Structure of Turbulent Shear Flow, 2nd edn. Cambridge University Press, New York
Violato D, Scarano F (2011) Three-dimensional evolution of flow structures in transitional circular and chevron jets. Phys Fluids 23(124104):1–25
Wieneke B (2008) Volume self-calibration for 3D particle image velocimetry. Exp Fluids 45:549–556
Worth Na, Nickels TB, Swaminathan N (2010) A tomographic PIV resolution study based on homogeneous isotropic turbulence DNS data. Exp Fluids 49:637–656
Yule aJ (1978) Large-scale structure in the mixing layer of a round jet. J Fluid Mech 89(3):413–433
Zaman KBMQ (1996) Axis switching and spreading of an asymmetric jet: the role of coherent structure dynamics. J Fluid Mech 316:1–27